Porous Materials

DOI: 10.1002/ange.201003163

Ionic Liquids as Versatile Precursors for Functionalized Porous Carbon and Carbon–Oxide Composite Materials by Confined Carbonization**

*Xiqing Wang and Sheng Dai**

The unique features of ionic liquids (ILs), such as negligible vapor pressure and versatile solvation properties,[1] have rendered the wide use of ILs in many emerging areas, for example, as green solvents for synthesis,[2] as media for advanced separation,[3] and as novel electrolytes for energy applications.[4] In an effort to explore new applications of ILs, we and others recently proposed a new methodology for the synthesis of porous carbon materials based on task-specific ionic liquids (TSILs).[5] The essence of this approach lies in the incorporation of cross-linkable functional groups, such as nitrile, into the structures of TSILs and the thermal stability of TSILs before their polycondensation.[5,6] These special precursor-controlled thermolysis properties[7] thereby make it possible to employ TSILs as excellent precursors to produce functional carbon materials with controlled pore architectures.[5,8] The huge number of possible combinations of cations and anions would provide great opportunities for tailor-made porous carbon materials from ILs. However, carbonization of conventional ILs without any cross-linkable functional groups under N_2 and ambient pressure affords no carbon yield. This is because of the lack of stable intermediate polymeric structures and the formation of volatile vapors during thermal decomposition of such ILs.

Herein, we report a strategy for forming functional porous carbon and carbon–oxide composite materials from conventional ILs by confined carbonization. This method does not require the ILs to have cross-linkable groups but instead utilizes the space confinement of ILs inside oxide networks (e.g., silica and titania) to convert the ILs with no char residue into efficient carbon precursors with carbonization yields approaching the theoretical limits. Another interesting feature of this approach is that it allows a rational tuning of the pore structure of the corresponding carbon–oxide composites and the derived carbon materials, which ranges from microporous to mesoporous and macroporous architectures. Furthermore, other elements, such as nitrogen and boron, which are crucial to modify the physical and chemical properties of the carbon materials,[9] can also be easily doped into carbon frameworks by employing heteroatom-substituted ILs. Compared with the carbon materials derived from conventional precursors,[10] which usually require post-synthesis modification,[11] confined carbonization of ILs affords a simple way to prepare functional and alloyed porous carbon and porous carbon–oxide composite materials.[12]

The confinement of ILs inside oxide networks was achieved by a nonhydrolytic sol–gel process,[13] wherein ILs were used as effective solvents to form oxide-based monolithic nanocomposites with homogeneously dispersed ILs. The uniformity is achieved by means of the unique solvation environment offered by ILs through Coulombic interactions and the formation of nanoscopic phase separation. Herein, we demonstrate an example of confined pyrolysis of an IL within a silica network. IL-containing monolithic silica gels were prepared by sol–gel processing of tetraethyl orthosilicate (TEOS) in the presence of formic acid and an IL, such as 1-butyl-3-methylimidazolium bis(trifluoromethylsulfonyl)-imide ([Bmim][NTf_2], see structure in Figure 1D). Depending on the amount of [Bmim][NTf_2] used, silica-based gels were formed within 1–3 h. After aging and drying to evaporate volatile solvents, transparent and clear monolithic silica gels (see Figure 1) containing different amounts of IL were obtained. Carbonization was performed by heating the gels to 800 °C for 2 h under flowing N_2. The obtained silica–

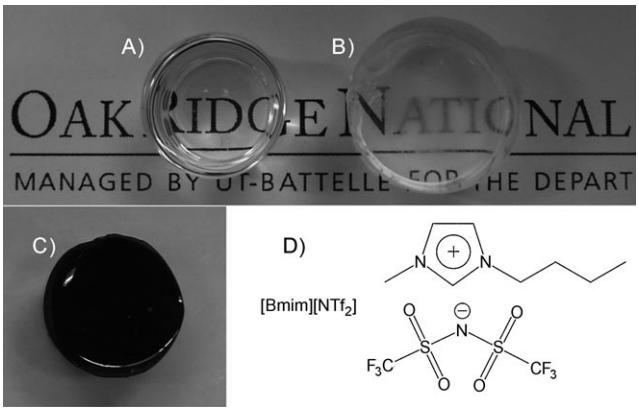

Figure 1. Transparent monolithic silica gels containing different amounts of [Bmim][NTf_2] ($x = 0.3$ and 2.0 for (A) and (B), respectively). After heat treatment under N_2, the clear monolith (A) turned black (C). D) Structure of [Bmim][NTf_2].

[*] Dr. X. Wang, Dr. S. Dai
Chemical Sciences Division, Oak Ridge National Laboratory
Oak Ridge, TN 37831 (USA)
Fax: (+1) 865-576-5235
E-mail: dais@ornl.gov

[**] This research was supported by the Division of Chemical Sciences, Biosciences, and Geosciences, Office of Basic Energy Sciences, U.S. Department of Energy under contract DE-AC05-OR22725 with Oak Ridge National Laboratory, managed and operated by UT-Battelle, LLC. We thank Dr. Huimin Luo and Dr. Gary A. Baker for providing ionic liquids, Dr. Miaofang Chi for high-resolution TEM, and Dr. Harry Meyer for XPS analysis.

Supporting information for this article is available on the WWW under http://dx.doi.org/10.1002/anie.201003163.

Online-Ausgabe unter wileyonlinelibrary.com

© 2010 Wiley-VCH Verlag GmbH & Co. KGaA, Weinheim

carbon composites were denoted as SC-BN-x ($x = 0.3$–2.0), where x represents the volume ratio of [Bmim][NTf_2]/TEOS used. Silica was removed by HF and the resulting carbon materials were denoted accordingly as C-BN-x.

The synthesis takes advantage of the excellent miscibility of [Bmim][NTf_2] with hydrophilic formic acid and hydrophobic TEOS, which gives a homogeneous clear mixture after gentle shaking. Considering the nonvolatility of [Bmim]-[NTf_2] and the fact that a negligible amount of the IL was found on the walls of the glass vial, we can conclude that the IL was completely trapped in the monolithic silica gels. Interestingly, after drying and curing, the gel containing less [Bmim][NTf_2] (Figure 1A) shows more shrinkage than the one containing more IL (Figure 1B). Our previous studies have shown that carbonization of an IL without any cross-linkable functional groups under N_2 and ambient pressure affords no carbon yield.[5a]

As expected, heat treatment of pure [Bmim][NTf_2] in nitrogen resulted in no char residue (Figure 2A, curve a).

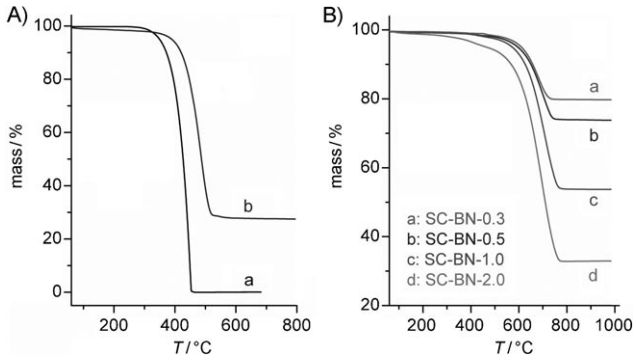

Figure 2. A) TGA curves of pure [Bmim][NTf_2] (a) and silica–[Bmim]-[NTf_2] gel (b) in N_2 with a heating rate of 2 °C min^{-1}. B) TGA curves of silica–carbon composites derived from gels containing different amounts of [Bmim][NTf_2] in air with a heating rate of 10 °C min^{-1}.

However, heating a [Bmim][NTf_2]-containing silica gel at 800 °C under the same conditions gave a black monolithic gel, clearly indicating the formation of a silica–carbon composite (Figure 1C). As a control experiment, heating a silica gel made the same way but without IL yielded colorless granules, thus suggesting that the carbon was derived from the IL. Moreover, thermogravimetric analysis (TGA) shows that the decomposition of [Bmim][NTf_2] within the silica gel (Figure 2A, curve b) started at around 400 °C, about 50 °C higher than the corresponding IL in the open space (Figure 2A, curve a). These results indicate that nanoconfinement of the IL not only improves its thermal stability but also increases the carbon yield, thus leading to the formation of silica–carbon composites. Clearly, nanoconfinement plays a key role in determining the course of the pyrolysis chemistry associated with ILs. The yield of aromatization through dehydrogenation reactions is considerably enhanced, while the evaporative loss of intermediate species (other than hydrogen gas) is suppressed.

The carbon contents of the silica–carbon composites were determined by TGA in air. As shown in Figure 2B, the more [Bmim][NTf_2] was incorporated into the silica gels, the higher was the weight loss of the TGA curves of the resulting silica–carbon composites. Table 1 lists the weight loss found by TGA

Table 1: Textural properties of silica–carbon composites and the derived carbon materials.

Materials	Weight loss [%][a]	S_{BET} [$m^2 g^{-1}$][b]	V_{total} [$cm^3 g^{-1}$][c]	V_{micro} [$cm^3 g^{-1}$][d]
SC-BN-0.3	19.7 (35.0)	155	0.30	0.06 (0.24)
SC-BN-0.5	25.3 (43.0)	169	0.25	0.07 (0.18)
SC-BN-1.0	45.6 (60.0)	247	0.22	0.10 (0.12)
SC-BN-2.0	65.4 (75.1)	359	0.25	0.16 (0.09)
C-BN-0.3	–	469	0.68	0.18 (0.50)
C-BN-0.5	–	420	0.65	0.17 (0.48)
C-BN-1.0	–	379	0.32	0.16 (0.16)
C-BN-2.0	–	358	0.24	0.16 (0.08)

[a] Weight loss of the TGA curves in air in the range of 200–800 °C. The numbers in parentheses are the carbon contents calculated theoretically from the amounts of IL used. [b] S_{BET}: Brunauer–Emmett–Teller (BET) surface area. [c] V_{total}: total pore volume. [d] V_{micro}: micropore volume, derived from the *D–R* plots. The numbers in parentheses are the porosity contributed from mesopores and macropores, as calculated by subtraction of the micropore volume from the total pore volume, $V_{total} - V_{micro}$.

for each silica–carbon composite as well as the carbon content calculated on the basis of the amount of IL incorporated into the silica gel. It can be seen that the more IL was used, the better the agreement between experimental and calculated values, which indicates an increase in carbonization yield. For example, the weight loss for SC-BN-2.0 was 65.4 wt %, close to the theoretical value (75.1 wt % based on carbon content).

Figure 3A and B show the scanning transmission electron microscopy (STEM) images of SC-BN-0.3, which reveal that the silica–carbon composite has a bicontinuous interconnected structure, a result of phase separation[13] occurring during the sol–gel process. That is, a solid phase of silica and a liquid phase of IL. The latter was transformed into a carbon phase after heating at high temperature in N_2. The silica and carbon phases can be distinguished by their morphology and surface roughness, as confirmed by line-scan energy-dispersive X-ray (EDX) analysis (Figure 3D). The silica phase has a smooth surface with a skeleton size of about 50–100 nm, while the carbon phase is composed of fused carbon nanoparticles with a rough surface.

STEM images also show obvious pores between the silica phase and the carbon phase, which range from about 20 to 50 nm in diameter. Removal of silica from the silica–carbon composites generated the corresponding porous carbon materials. A typical STEM image of C-BN-0.3 (Figure 3C) reveals a broad pore size distribution in the mesopore and macropore region (10–100 nm). The meso/macroporosity of carbon materials originates from that of the parent silica–carbon composite, the space left by removal of silica, and the interparticle pores between primary carbon particles. Such

 © 2010 Wiley-VCH Verlag GmbH & Co. KGaA, Weinheim

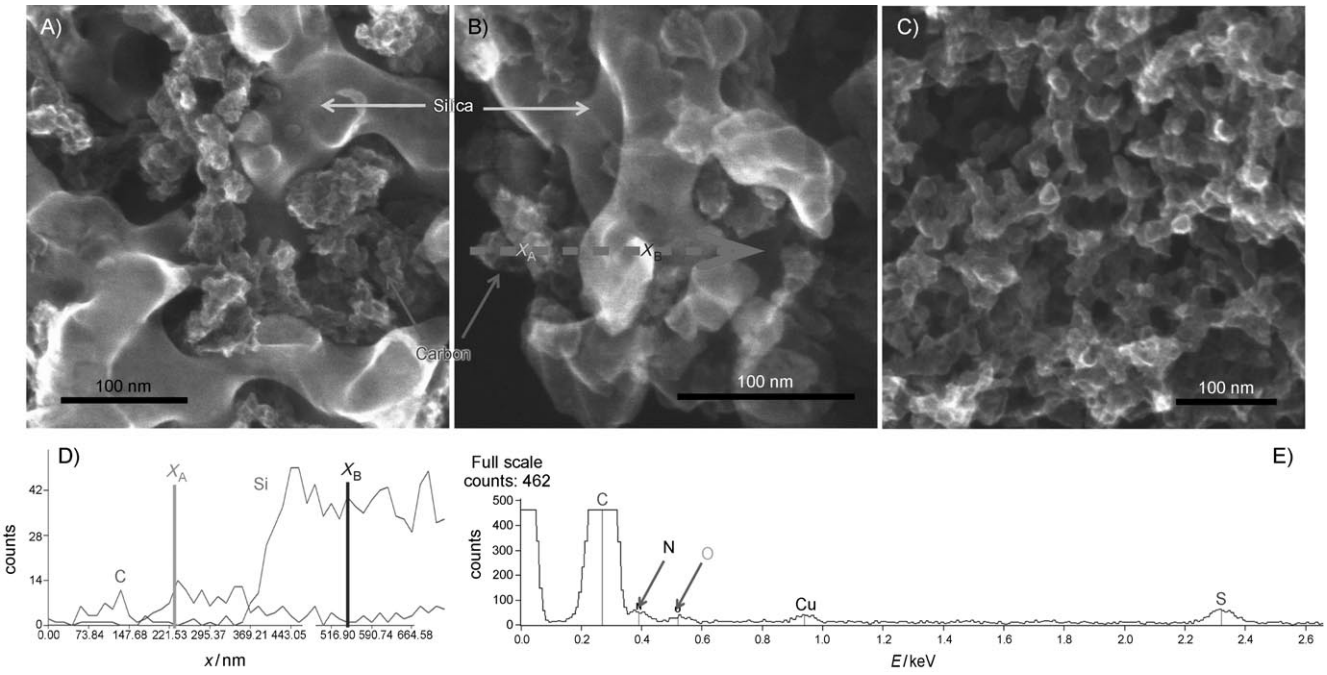

Figure 3. STEM images of A,B) SC-BN-0.3 and C) the derived carbon C-BN-0.3. The dotted arrow in (B) shows the direction of a line-scan EDX analysis of SC-BN-0.3. D) The line scan reveals the nature of mainly carbon and silica at spots x_A and x_B, respectively. E) EDX spectrum of C-BN-0.3 on a rectangular region of image (C).

primary carbon particles are around 10–50 nm in size and mainly microporous, as revealed by the high-resolution TEM images (Figure 4). The EDX spectrum of C-BN-0.3 (Figure 3E) suggests the complete removal of silica and the

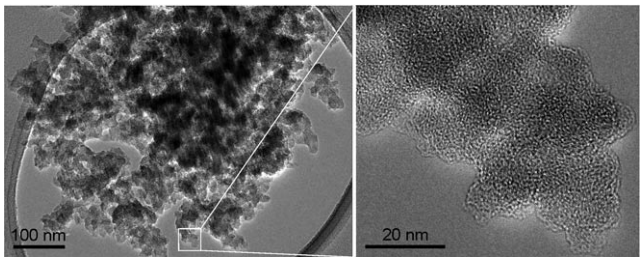

Figure 4. High-resolution TEM images of C-BN-0.3.

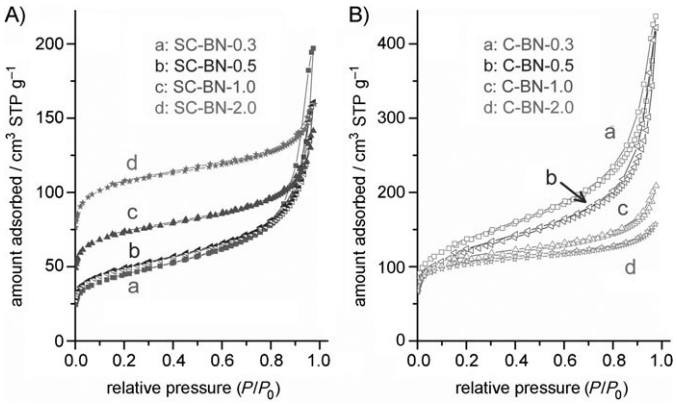

Figure 5. N_2 adsorption–desorption isotherms of A) silica–carbon composites and B) the derived porous carbons after removal of silica.

presence of certain amounts of heteroatoms, such as nitrogen and sulfur, all of which come from the IL. X-ray photoelectron spectroscopy (XPS) analysis of C-BN-0.3 shows the contents of nitrogen and sulfur are 10.6 and 1.2 at%, respectively (Figure S1 and Table S1 in the Supporting Information). XPS measurements of other carbon materials show similar results.

Figure 5 shows the N_2 adsorption–desorption isotherms of the silica–carbon composites as well as their carbon derivatives. Pronounced capillary condensation steps were found at relative pressures of 0.85–1.0, thus indicating the presence of large mesopores and macropores, which agrees well with the observations by STEM and high-resolution TEM. Interestingly, as more [Bmim][NTf_2] was used, the obtained silica–carbon composites became less mesoporous but more microporous (see also Table 1). For example, the composite SC-BN-2.0 exhibited the highest BET surface area and the largest micropore volume but the lowest meso/macropore volume. However, the derived carbon materials followed a trend of decreasing BET surface area with increasing amount of [Bmim][NTf_2], the reverse of the behavior observed with the parent silica–carbon composites. Although all carbon materials exhibited almost identical microporosity, they differed greatly in meso/macroporosity, and ranged from high meso/macropore volume for C-BN-0.3 to mainly microporosity for

 © 2010 Wiley-VCH Verlag GmbH & Co. KGaA, Weinheim

C-BN-2.0 (Table 1). Such a sharp difference in textural properties of the silica–carbon composites and carbon materials can be attributed to the variation of phase separation within the gels containing different amounts of IL.[13] These results demonstrate the feasibility of control over the pore architecture of the silica–carbon composites and carbon materials by simply varying the amount of IL used as a solvent.

In addition to [Bmim][NTf_2], other ILs, such as 1-ethyl-3-methylimidazolium tetracyanoborate ([Emim][$B(CN)_4$]), have also been used to prepare porous silica–carbon composites and thereafter nitrogen- and boron-functionalized carbon materials (see XPS results in the Supporting Information). The method also allows us to make porous titania–carbon composites. Figure 6 shows the XRD pattern of a

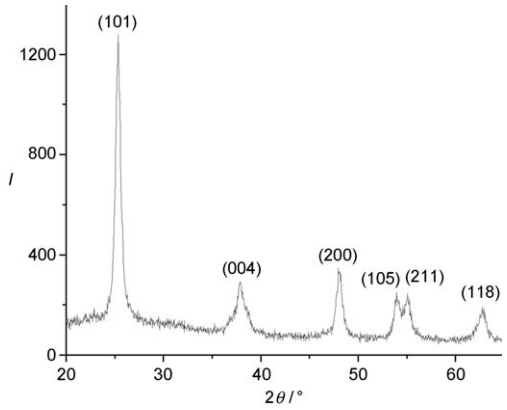

Figure 6. XRD pattern of a carbon–anatase nanocomposite.

porous carbon–anatase composite (C/TiO_2-BN-0.5, see the STEM images in the Supporting Information). These results indicate that the method reported herein is versatile and general enough to produce functional porous carbon materials and porous carbon–oxide composites with potential for use in many areas, for example, as electrode materials for lithium-ion batteries and supercapacitors.[14]

In summary, a general approach towards functionalized porous carbon and porous carbon–oxide composite materials with controlled pore architectures has been developed by the confined and oxide-catalyzed carbonization of ILs trapped within an oxide framework, which can be easily fabricated by nonhydrolytic sol–gel processing using ILs as solvents.

Experimental Section

Synthesis: Typically, TEOS (1.0 mL) was mixed with [Bmim][NTf_2] (0.3–2.0 mL) in a glass vial, followed by the addition of formic acid (1.0 mL). Depending on the amount of [Bmim][NTf_2] used, silica-based gels were formed within 1–3 h. After aging and drying to evaporate volatile solvents, transparent and clear monolithic silica gels containing different amounts of IL were obtained. Carbonization was performed by heating the gels to 800 °C for 2 h at a heating rate of 2 °C min^{-1} under flowing N_2. Carbon–titania composites were prepared in a similar way. In a typical synthesis, titanium butoxide ($Ti(OBu)_4$; 1.0 mL) was mixed with [Bmim][NTf_2] (0.5 mL) in a glass vial, followed by the addition of acetic acid (1.0 mL) and formic acid (0.1 mL). After aging and drying at room temperature overnight, the gel was cured at 100 °C for 24 h. Heat treatment was carried out at 600 °C for 4 h at a heating rate of 2 °C min^{-1} under flowing N_2. The obtained carbon–titania composite was denoted as C/TiO_2-BN-0.5.

Characterization: N_2 sorption isotherms were recorded on a Micromeritics Tristar analyzer at −196 °C (77 K). Prior to measurement, the sample was purged with flowing N_2 at 150 °C for 3 h. The specific surface area was calculated using the BET method from the nitrogen adsorption data in the relative range (P/P_0) of 0.05–0.20. The total pore volume (V_{total}) was determined from the amount of N_2 uptake at $P/P_0 = 0.95$. The micropore volume (V_{micro}) was estimated using the Dubinin–Radushkevich plots. The meso/macropore volume was calculated by subtraction of the micropore volume from the total pore volume ($V_{meso+macro} = V_{total} - V_{micro}$). STEM images were obtained on a Hitachi HD-2000 STEM microscope operating at 200 kV under the SE and TE modes. High-resolution TEM images were taken on an FEI Titan microscope operating at 300 kV. Each image was recorded from an area without prebeam illumination to minimize any possible beam irradiation. The XRD pattern of C/TiO_2-BN-0.5 was recorded on a Siemens D5005 diffractometer operating at 40 kV and 40 mA. XPS experiments were run on a Thermo Fisher Scientific K-Alpha XPS instrument. Survey scans were obtained using a pass energy of 200 eV, while high-energy-resolution scans of specific elements were obtained using a 50 eV pass energy.

Received: May 25, 2010
Published online: August 2, 2010

Keywords: carbon · carbon–oxide composites · ionic liquids · mesoporous materials · microporous materials

[1] a) T. Welton, *Chem. Rev.* **1999**, *99*, 2071; b) P. Wasserscheid, W. Keim, *Angew. Chem.* **2000**, *112*, 3926; *Angew. Chem. Int. Ed.* **2000**, *39*, 3772.
[2] a) Z. Ma, J. H. Yu, S. Dai, *Adv. Mater.* **2010**, *22*, 261; b) M. Antonietti, D. B. Kuang, B. Smarsly, Z. Yong, *Angew. Chem.* **2004**, *116*, 5096; *Angew. Chem. Int. Ed.* **2004**, *43*, 4988.
[3] X. Han, D. W. Armstrong, *Acc. Chem. Res.* **2007**, *40*, 1079.
[4] a) M. Armand, F. Endres, D. R. MacFarlane, H. Ohno, B. Scrosati, *Nat. Mater.* **2009**, *8*, 621; b) D. R. Macfarlane, M. Forsyth, P. C. Howlett, J. M. Pringle, J. Sun, G. Annat, W. Neil, E. I. Izgorodina, *Acc. Chem. Res.* **2007**, *40*, 1165.
[5] a) J. S. Lee, X. Q. Wang, H. M. Luo, G. A. Baker, S. Dai, *J. Am. Chem. Soc.* **2009**, *131*, 4596; b) J. S. Lee, X. Q. Wang, H. M. Luo, S. Dai, *Adv. Mater.* **2010**, *22*, 1004; c) J. P. Paraknowitsch, J. Zhang, D. S. Su, A. Thomas, M. Antonietti, *Adv. Mater.* **2010**, *22*, 87.
[6] T. J. Wooster, K. M. Johanson, K. J. Fraser, D. R. MacFarlane, J. L. Scott, *Green Chem.* **2006**, *8*, 691.
[7] a) L. Zhi, J. J. Wang, G. L. Cui, M. Kastler, B. Schmaltz, U. Kolb, U. Jonas, K. Mullen, *Adv. Mater.* **2007**, *19*, 1849; b) L. J. Zhi, Y. S. Hu, B. El Hamaoui, X. Wang, I. Lieberwirth, U. Kolb, J. Maier, K. Mullen, *Adv. Mater.* **2008**, *20*, 1727.
[8] J. S. Lee, H. M. Luo, G. A. Baker, S. Dai, *Chem. Mater.* **2009**, *21*, 4756.
[9] a) Y. Wang, J. S. Zhang, X. C. Wang, M. Antonietti, H. R. Li, *Angew. Chem.* **2010**, *122*, 3428; *Angew. Chem. Int. Ed.* **2010**, *49*, 3356; b) Y. J. Zhang, T. Mori, J. H. Ye, M. Antonietti, *J. Am. Chem. Soc.* **2010**, *132*, 6294.
[10] a) Z. J. Li, M. Jaroniec, *Carbon* **2001**, *39*, 2080; b) M. Kruk, K. M. Kohlhaas, B. Dufour, E. B. Celer, M. Jaroniec, K. Matyjaszewski, R. S. Ruoff, T. Kowalewski, *Microporous Mesoporous Mater.* **2007**, *102*, 178; c) A. H. Lu, A. Kiefer, W. Schmidt, F. Schüth, *Chem. Mater.* **2004**, *16*, 100; d) A. H. Lu, W. C. Li, G. P. Hao, B.

 © 2010 Wiley-VCH Verlag GmbH & Co. KGaA, Weinheim

Spliethoff, H. J. Bongard, B. B. Schaack, F. Schüth, *Angew. Chem.* **2010**, *122*, 1659; *Angew. Chem. Int. Ed.* **2010**, *49*, 1615.
[11] a) C. D. Liang, Z. J. Li, S. Dai, *Angew. Chem.* **2008**, *120*, 3754; *Angew. Chem. Int. Ed.* **2008**, *47*, 3696; b) A. Stein, Z. Y. Wang, M. A. Fierke, *Adv. Mater.* **2009**, *21*, 265.
[12] a) J. Gorka, M. Jaroniec, *J. Phys. Chem. C* **2008**, *112*, 11657; b) G. P. Hao, W. C. Li, D. Qian, A. H. Lu, *Adv. Mater.* **2010**, *22*, 853; c) B.-H. Han, W. Z. Zhou, A. Sayari, *J. Am. Chem. Soc.* **2003**, *125*, 3444.
[13] S. Dai, Y. H. Ju, H. J. Gao, J. S. Lin, S. J. Pennycook, C. E. Barnes, *Chem. Commun.* **2000**, 243.
[14] a) L. L. Zhang, X. S. Zhao, *Chem. Soc. Rev.* **2009**, *38*, 2520; b) T. R. Demir-Cakan, Y. S. Hu, M. Antonietti, J. Maier, M. M. Titirici, *Chem. Mater.* **2008**, *20*, 1227; c) X. L. Feng, Y. Y. Liang, L. J. Zhi, A. Thomas, D. Q. Wu, I. Lieberwirth, U. Kolb, K. Müllen, *Adv. Funct. Mater.* **2009**, *19*, 2125.

 © 2010 Wiley-VCH Verlag GmbH & Co. KGaA, Weinheim